Collective effects of XMAP215, EB1, CLASP2, and MCAK lead to robust microtubule treadmilling

Göker Arpağ[a,1], Elizabeth J. Lawrence[a,1], Veronica J. Farmer[a], Sarah L. Hall[a], and Marija Zanic[a,b,c,2]

[a]Department of Cell and Developmental Biology, Vanderbilt University, Nashville, TN 37240; [b]Department of Chemical and Biomolecular Engineering, Vanderbilt University, Nashville, TN 37235; and [c]Department of Biochemistry, Vanderbilt University, Nashville, TN 37205

Edited by Rebecca Heald, University of California, Berkeley, CA, and approved April 23, 2020 (received for review February 19, 2020)

Microtubule network remodeling is essential for fundamental cellular processes including cell division, differentiation, and motility. Microtubules are active biological polymers whose ends stochastically and independently switch between phases of growth and shrinkage. Microtubule treadmilling, in which the microtubule plus end grows while the minus end shrinks, is observed in cells; however, the underlying mechanisms are not known. Here, we use a combination of computational and in vitro reconstitution approaches to determine the conditions leading to robust microtubule treadmilling. We find that microtubules polymerized from tubulin alone can treadmill, albeit with opposite directionality and order-of-magnitude slower rates than observed in cells. We then employ computational simulations to predict that the combinatory effects of four microtubule-associated proteins (MAPs), namely EB1, XMAP215, CLASP2, and MCAK, can promote fast and sustained plus-end-leading treadmilling. Finally, we experimentally confirm the predictions of our computational model using a multi-MAP, in vitro microtubule dynamics assay to reconstitute robust plus-end-leading treadmilling, consistent with observations in cells. Our results demonstrate how microtubule dynamics can be modulated to achieve a dynamic balance between assembly and disassembly at opposite polymer ends, resulting in treadmilling over long periods of time. Overall, we show how the collective effects of multiple components give rise to complex microtubule behavior that may be used for global network remodeling in cells.

microtubule | treadmilling | dynamic instability | microtubule-associated proteins | in vitro reconstitution

Treadmilling is an evolutionarily conserved, nonequilibrium behavior of cytoskeletal filaments entailing simultaneous assembly at one polymer end and disassembly at the other end. Treadmilling is a quintessential property of dynamic actin filaments and is critical for cell motility in eukaryotic cells (1). In bacterial systems, treadmilling of both actin-like and microtubule-like polymers drives cell division and intracellular transport (2–5). In contrast, the hallmark behavior of microtubules is "dynamic instability" (6), where the microtubule plus and minus ends in vitro independently switch between phases of assembly and disassembly through transitions known as catastrophe and rescue. Cellular studies of microtubule dynamics are commonly restricted to microtubule plus ends, as the minus ends are typically considered to be anchored or capped (7). However, it is becoming increasingly apparent that minus ends can be both free and dynamic in the cytoplasm. Moreover, in situations where minus ends are not stabilized, microtubules can treadmill with growing plus ends and shrinking minus ends (8–19). For example, microtubule treadmilling has been observed in the cortex of epithelial cells (10), in cytoplasmic fragments of fish melanophores (8), in *Drosophila* S2 cells upon depletion of a minus-end capping protein Patronin (13), and in microtubule cortical arrays in plants (9). In these systems, free minus ends were generated in a variety of ways including microtubule buckling and breakage (10), severing (14), de novo nucleation (9), and release from nucleation sites (8) and also destabilized through the action of microtubule depolymerases (13). Furthermore, microtubule treadmilling by polymerization at kinetochores and depolymerization at spindle poles have been implicated in poleward microtubule flux within the mitotic spindle (20). In all of these contexts, treadmilling may present a distinct mechanism for microtubule turnover and can function in overall microtubule network reorganization (9).

Earlier in vitro studies with purified tubulin investigated the conditions required for microtubule treadmilling (21–27). While microtubule treadmilling events were directly observed in some cases, the rates and the directionality were very different from those measured in cells (24, 25, 27). In cells, microtubule dynamics are regulated by a complex network of microtubule-associated proteins (MAPs) that can alter microtubule growth or shrinkage rates, modulate catastrophe or rescue frequencies, and generally stabilize or destabilize microtubule polymers. A number of MAPs are specifically targeted to microtubule ends and can have preferential localization at one or the other end (28). Thus, in principle, differential modulation of microtubule dynamics at the two ends can lead to the observed microtubule treadmilling in cells. Nevertheless, due to the complex interplay between the biochemical regulation of microtubule ends and the large network of regulatory factors in cells, the conditions leading to microtubule treadmilling have remained obscure.

Significance

Treadmilling is a complex behavior of active polymers characterized by polymerization at one polymer end and simultaneous depolymerization at the other end. Treadmilling is an essential feature of cytoskeletal filaments driving actin-based cell motility, bacterial cell division and transport, and reorganization of microtubule arrays in plants. Although microtubule treadmilling occurs in many cellular contexts, how cells coordinate growth at microtubule plus ends and shrinkage at microtubule minus ends to achieve treadmilling is not understood. Here, we employ predictive computational modeling and a multiprotein in vitro assay to reconstitute cellular-like microtubule treadmilling. Our work provides a deeper understanding of how active polymer systems can be tuned to give rise to robust yet dynamic cytoskeletal architectures.

Author contributions: G.A., E.J.L., and M.Z. designed research; G.A. and E.J.L. performed research; G.A., E.J.L., V.J.F. and S.L.H. contributed new reagents/analytic tools; G.A., E.J.L., and M.Z. analyzed data; and G.A., E.J.L. and M.Z. wrote the paper.

The authors declare no competing interest.

This article is a PNAS Direct Submission.

Data deposition: All simulation codes used in this study are available on GitHub (https://github.com/ZanicLab).

[1]G.A. and E.J.L. contributed equally to this work.

[2]To whom correspondence may be addressed. Email: marija.zanic@vanderbilt.edu.

This article contains supporting information online at https://www.pnas.org/lookup/suppl/doi:10.1073/pnas.2003191117/-/DCSupplemental.

First published May 26, 2020.

Results

Population Measurements of Microtubule Dynamics Predict Treadmilling with Minus-End Directionality. To identify the conditions that would permit microtubule treadmilling, we first investigated microtubule dynamics over a range of tubulin concentrations, revisiting a classic study by Walker et al. (29). Dynamic microtubule extensions were grown from GMPCPP-stabilized "seeds" with fluorescently labeled tubulin and imaged by total internal reflection fluorescence (TIRF) microscopy (30) (Fig. 1*A*). The rates of growth and shrinkage and the frequencies of rescue and catastrophe were quantified at both microtubule ends by kymograph analysis (31) (Fig. 1 *B*–*F*). Using these population-level measurements, we calculated the net polymer length gain/loss for each end (also referred to as net subunit "flux") (29, 32, 33):

$$J_{Analytical} = v_g p_g - v_s p_s = \frac{v_g f_{res} - v_s f_{cat}}{f_{res} + f_{cat}},$$

where v_g and v_s are growth and shrinkage rates, p_g and p_s are fractions of time spent in growth and shrinkage phases, and f_{res} and f_{cat} are rescue and catastrophe frequencies, all independently measured for microtubule plus and minus ends (Fig. 1*G* and also see *Materials and Methods*). Analysis of the plus- and minus-end flux rates revealed a range of tubulin concentrations (Fig. 1*G*, shaded region, 3.7 to 6.9 μM; see *Materials and Methods*) for which the minus ends are predicted to exhibit net growth (positive flux), while the plus ends are predicted to exhibit net shrinkage (negative flux), consistent with previous reports (29, 32). This observation identified a potential regime for microtubule treadmilling with minus-end-leading directionality.

Individual Microtubules Grown with Tubulin Alone Can Display Treadmilling with Low Flux Rates. To investigate whether individual microtubules display treadmilling when grown in the conditions identified by our population-level measurements, we modified the in vitro dynamics assay to exclude stabilized seeds, which inherently prevent microtubule treadmilling (Fig. 2*A*). Here, microtubules were nucleated using guanosine-5′-triphosphate (GTP)-tubulin and bound to coverslips with rigor kinesin-1 motors (*Materials and Methods*); this approach had no significant effect on microtubule dynamics (*SI Appendix*, Table S1). The tubulin solution was then exchanged for a lower concentration of GTP-tubulin with a distinct fluorescent label (6 μM), matching the predicted treadmilling regime (Fig. 1*G*). The net subunit flux was measured at steady-state total polymer length (*SI Appendix*, Fig. S1) for each microtubule end by dividing the total polymer length gain/loss by the observation time:

$$J_{Empirical} = \frac{x_f - x_i}{t_f - t_i} = \frac{\Delta x}{\Delta t},$$

where x_i and x_f are the initial and final position of a given end at times t_i and t_f, respectively. All observed polymers displayed catastrophe and rescue transitions consistent with microtubule dynamic instability. We then classified each microtubule into one of four distinct dynamic modes based on the net flux at each end: 1) both ends growing; 2) plus-end-leading treadmilling (net plus-end growth and minus-end shrinkage); 3) minus-end-leading treadmilling (net plus-end shrinkage and minus-end growth); and 4) both ends shrinking (Fig. 2*B*; also see *Materials and Methods* and *SI Appendix*, Fig. S1). Based on this classification, 48% of microtubules (88 out of 183) were treadmilling, of which 85% (75 out of 88) displayed minus-end-leading treadmilling (Fig. 2*C*), in agreement with a previous report (24). The average flux was 0.48 ± 0.52 nm/s for minus ends and 0.0 ± 1.9 nm/s for plus ends (mean ± SD, n = 183) (Fig. 2*D*), consistent with the rates we obtained from the population-level measurements (Fig. 1*G*). Thus, our population-level measurements successfully predicted a condition permissive for minus-end-leading treadmilling of individual microtubules.

Simulations Predict That Robust Plus-End-Leading Treadmilling Can Be Induced by a Combination of MAPs. Our experiments revealed that microtubules grown with tubulin alone can treadmill; however, in contrast to cellular observations, treadmilling microtubules in vitro displayed an order-of-magnitude lower fluxes and predominantly minus-end directionality. We hypothesized that

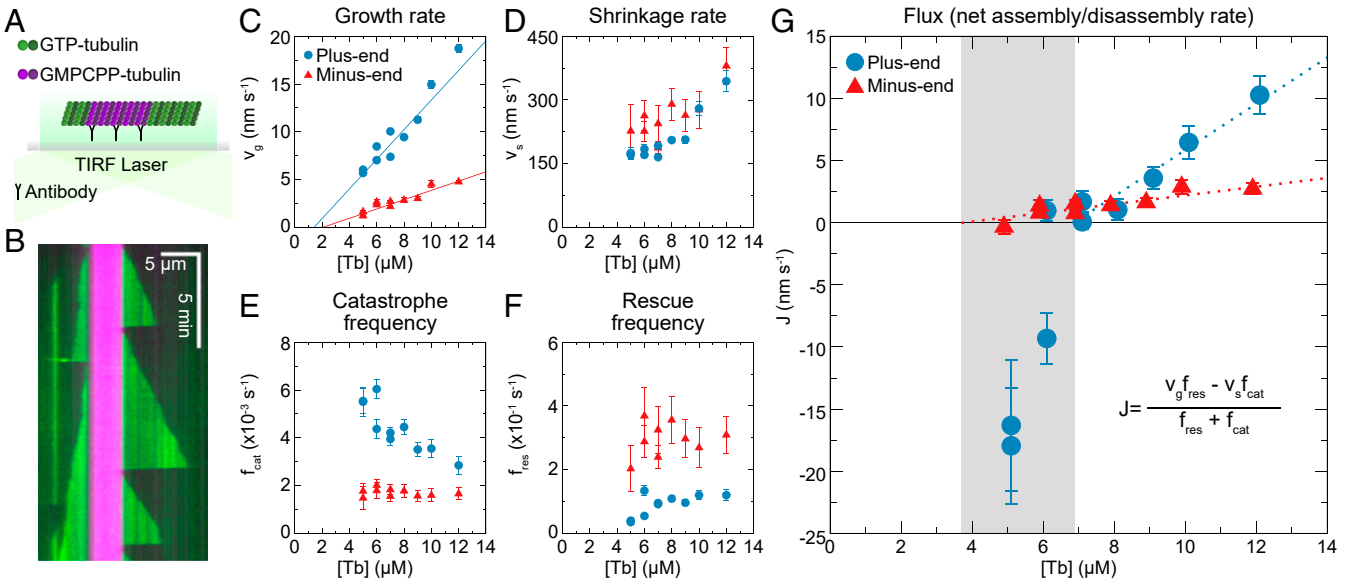

Fig. 1. Population-level measurements predict microtubule treadmilling with leading minus ends. (*A*) Schematic of the assay used to study the dynamics of GTP-tubulin extensions grown from GMPCPP-stabilized microtubule seeds using TIRF microscopy. (*B*) Representative kymograph showing dynamic microtubule extensions (green) growing from a stable microtubule "seed" (magenta). Quantification of (*C*) growth rate, (*D*) shrinkage rate, (*E*) catastrophe frequency, and (*F*) rescue frequency of both microtubule ends over a range of tubulin concentrations. (*G*) Analytically calculated flux (net assembly/disassembly rate) on microtubule ends as a function of tubulin concentration. Blue and red lines are weighted linear fits in *C* and *G*. The area highlighted in gray indicates a range of tubulin concentrations consistent with minus-end-leading treadmilling behavior (*Materials and Methods*). Error bars are SEM.

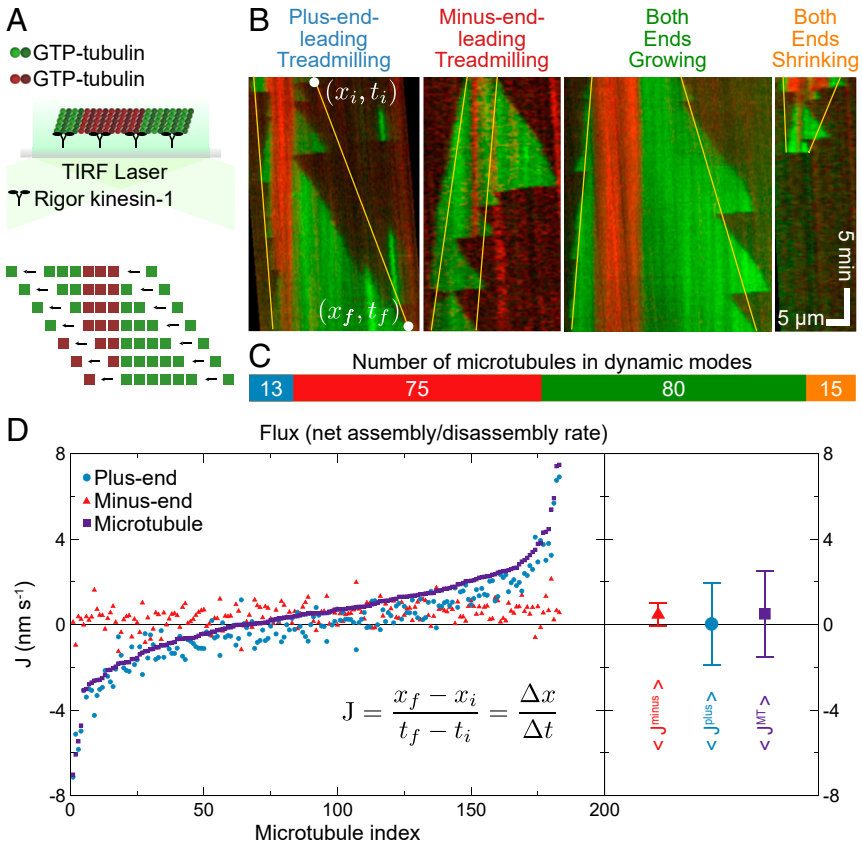

Fig. 2. Individual microtubules grown with tubulin alone can treadmill in vitro. (*A*) Schematic of a "seedless" assay that permits individual polymer treadmilling. (*B*) Representative kymographs showing examples of distinct dynamic modes used for classification. Yellow lines show the net flux at each microtubule end. (*C*) Color bar shows the number of microtubules observed in each dynamic mode (total $n = 183$). (*D*) Measured flux values at individual microtubule plus and minus ends. Fluxes at given ends were determined empirically by dividing the net length gain/loss by observation time. Net length gain is associated with positive flux and net length loss with negative flux. The total flux on a given microtubule is the sum of the fluxes at its plus and minus ends. (*Right*) Mean (±SD) of the individual fluxes ($n = 183$). Observation times ranged from 10 to 35 min, with a median of 33.8 min (29.4 ± 7.3 min, mean ± SD). Initial polymer lengths at the beginning of analysis ranged between 0.4 μm and 26.0 μm, with median of 4.6 μm (5.4 ± 3.4 μm, mean ± SD). Data were obtained from three independent experiments.

the action of regulatory MAPs drives the robust plus-end-leading treadmilling observed in cells. Furthermore, we anticipated that cellular-like treadmilling can only be achieved through a complex interplay of multiple MAPs, simultaneously regulating both microtubule ends. For this reason, we employed computational simulations to explore how ensembles of MAPs may promote treadmilling (*Materials and Methods* and *SI Appendix*, Fig. S2). We based our simulations at the lower end of soluble tubulin concentrations in the predicted treadmilling regime (4 μM; Fig. 1*G*), in which minus-end flux approaches zero, predisposing minus ends for disassembly (Fig. 3 *A* and *B*, *SI Appendix*, Table S2, and Movie S1). We then increased the complexity in our simulations by sequentially introducing MAPs constrained by published experimental results on the effects of both individual and combinations of MAPs on microtubule dynamics.

First, we sought to increase the plus-end growth rate in our simulations to the levels typically observed in cells. XMAP215 is a well-known microtubule polymerase that specifically promotes microtubule plus-end growth (34, 35). In addition, XMAP215 synergizes with microtubule end-binding protein EB1 to further increase microtubule growth rates in vitro (36). Although the dominant effect of combining XMAP215 with EB1 is an increase in the plus-end growth rate, a simultaneous increase in plus-end catastrophe frequency was also observed (36). We simulated the addition of XMAP215 and EB1 to the seedless microtubule dynamics assay, taking all of the experimentally determined parameters into account. We found that the majority of simulated microtubules depolymerized completely within a few minutes (2.4 ± 1.2 min, mean ± SD, $n = 96$) despite the fast plus-end growth rates, due to the relatively high catastrophe frequency and minimal rescues (Fig. 3*A*, *SI Appendix*, Table S2, and Movie S2). Thus, the net subunit flux at the plus ends in simulations with XMAP215 and EB1 was even more negative than the tubulin-alone condition; as a result, the majority of simulated microtubules were still classified as minus-end-leading treadmilling (Fig. 3 *B* and *C*).

To prevent complete polymer loss induced by the onset of plus-end catastrophe, we next introduced CLASP2 into our in silico assay. Members of the CLASP family are targeted to microtubule plus ends via a direct interaction with EB1, where they specifically lower catastrophe and increase rescue frequency, without significantly altering the microtubule growth rates (37–39). Our simulations of dynamic microtubules with XMAP215, EB1, and CLASP2 resulted in high net plus-end flux rates, comparable to those previously reported in cells, and the overall prevention of polymer loss (Fig. 3 *A* and *B*, *SI Appendix*, Table S2, and Movie S3). However, although a large fraction of the in silico microtubules in this condition were classified as plus-end-leading treadmilling (Fig. 3*C*), almost half of the microtubule population exhibited both-ends-growing behavior, due to the small but positive subunit flux at the minus end.

To shift the majority of the microtubule population into plus-end-leading treadmilling regime, we next sought conditions

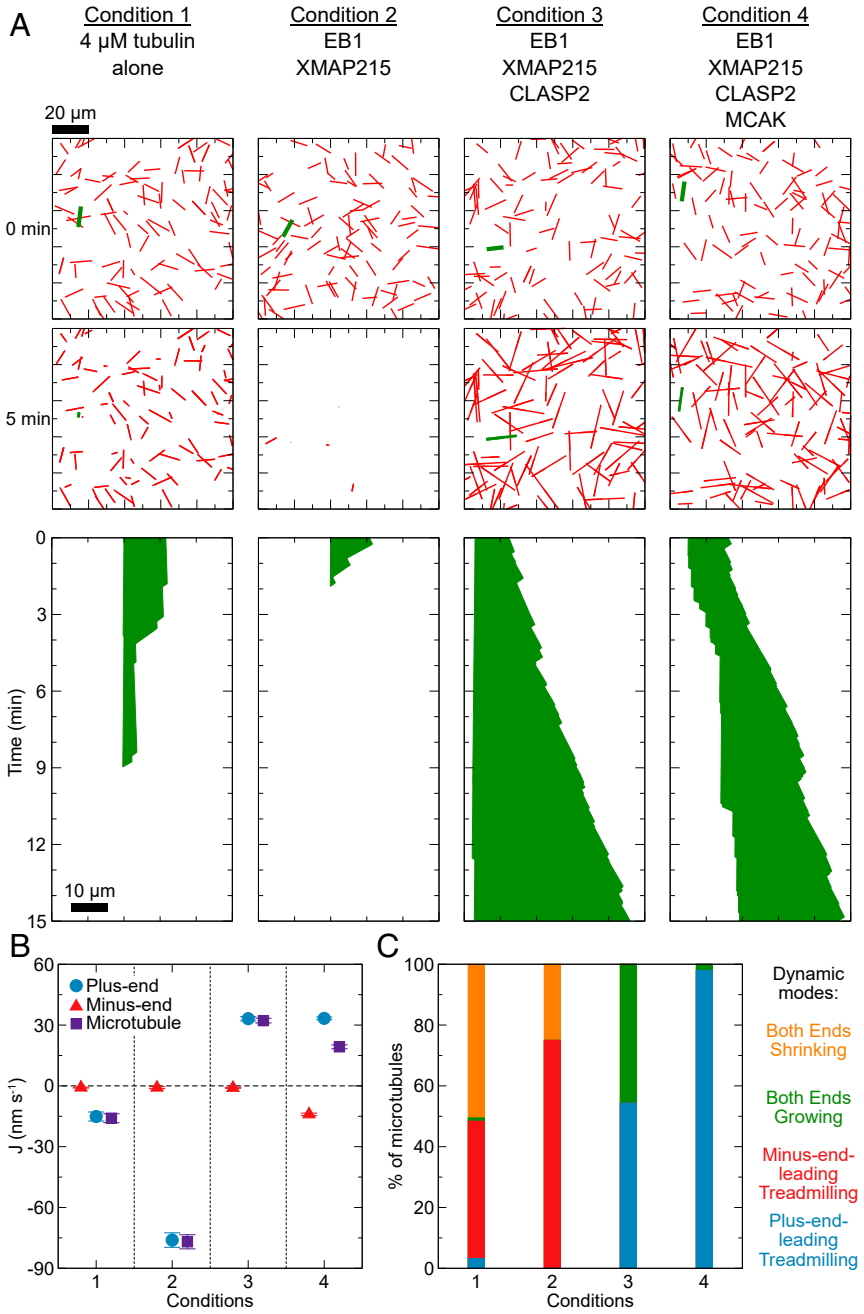

Fig. 3. Simulations predict robust plus-end-leading treadmilling in the presence of MAPs. (*A*) Simulated conditions with different combinations of MAPs. The top two rows show fields of view at 0 min and at 5 min of simulation time. Green microtubules are chosen for example kymographs (bottom row), while the rest of the polymers are shown in red. (*B*) Average net flux rates showing the effects of MAPs in the seedless assay. Error bars are SEM (n = 93, 96, 81, and 95 for conditions 1 through 4, respectively). (*C*) Classification of simulated microtubules into four different dynamic modes. n = 100 microtubules were simulated for each condition at the start of simulations. The longest duration that both ends of a given microtubule remained within the field of view was used to determine the empirical flux rates and classify dynamic modes. Microtubules observed for less than 30 s were discarded. See *SI Appendix*, Table S2 for further details.

that would promote minus-end depolymerization. We hypothesized that including a potent minus-end depolymerase would increase the frequency of minus-end catastrophe, leading to microtubule depolymerization and overall negative flux at the minus end. MCAK, a kinesin-13 motor, is a well-studied microtubule depolymerase which promotes catastrophe and depolymerizes both microtubule ends (40–42). A recent study found that the presence of CLASP at microtubule plus ends protects against MCAK's destabilizing activity (38). Given that CLASP is targeted to microtubule ends through its interaction with EB1 (37), and that EB1's localization increases with the increasing growth rate (43, 44), we expect that the protective effect of CLASP will be restricted to the fast-growing microtubule plus ends. Therefore, we simulated the addition of MCAK to XMAP215, EB1, and CLASP2 to specifically affect microtubule minus ends (Fig. 3*A*, *SI Appendix*, Table S2, and Movie S4). Our simulations resulted in negative minus-end flux (−14.1 ± 0.6 nm/s, mean ± SEM, n = 95), with the vast majority (98%) of in silico microtubules exhibiting plus-end-leading treadmilling behavior (Fig. 3 *B* and *C*, condition 4). Importantly, and as expected,

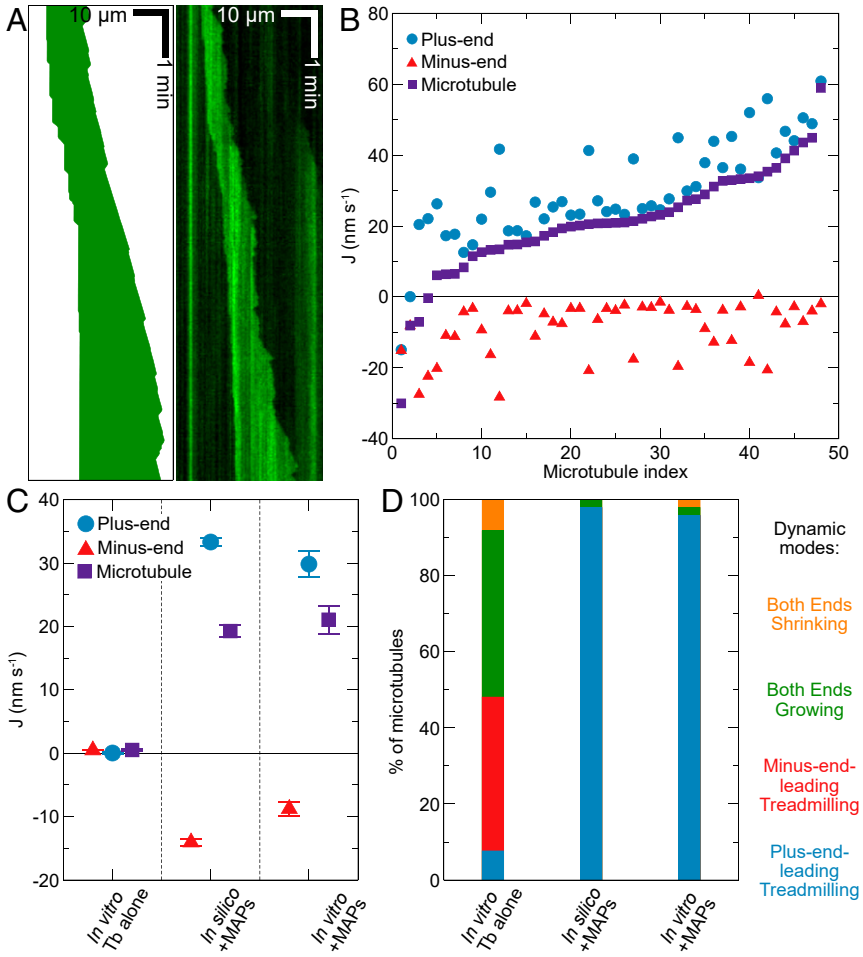

Fig. 4. Reconstitution of robust plus-end-leading treadmilling in vitro. (*A*) Representative kymographs of a simulated (*Left*) and in vitro (*Right*) microtubule in the presence of XMAP215, EB1, CLASP2, and MCAK. (*B*) Empirically measured fluxes of individual microtubules in vitro. Observation times ranged from 2 to 30 min, with median of 12.4 min (14.6 ± 9.3 min, mean ± SD). (*C*) Average net flux rates comparing tubulin alone in vitro, multicomponent in silico, and multicomponent in vitro experiments in the presence of MAPs. Error bars are SEM (n = 183, 95, and 48, respectively). In vitro data in the presence of MAPs were obtained from four independent experiments. (*D*) Percentage of microtubules classified into distinct dynamic modes, comparing the three conditions as in *C*.

simulating each of the four MAPs individually, using the experimentally determined effects on microtubule dynamics (34, 36, 37, 42, 44), did not yield large positive plus-end flux values, necessary for the robust plus-end-leading treadmilling behavior (*SI Appendix*, Fig. S3). In contrast, combining the known effects of XMAP215, EB1, CLASP2, and MCAK in our seedless in silico microtubule dynamics assay predicted a regime for robust plus-end-leading microtubule treadmilling.

Multicomponent In Vitro Experiments Demonstrate Robust Plus-End-Leading Microtubule Treadmilling. Having successfully demonstrated conditions leading to plus-end-directed treadmilling with MAPs in silico, we next set out to experimentally validate our in silico predictions using the in vitro seedless reconstitution assay. As before, we nucleated microtubules in the absence of MAPs then exchanged the reaction solution to include 4 μM tubulin and purified XMAP215, EB1, CLASP2, and MCAK proteins (*SI Appendix*, Fig. S4). We performed numerical analysis of flux sensitivity to dynamic parameters to guide our choice of protein concentrations (*SI Appendix*, Fig. S5 and Movie S5). We took advantage of the known effects of the MAPs on microtubule dynamics as a function of individual protein concentration (34, 36, 37, 42) to determine the protein concentrations that will yield the required activity of each MAP, as established in silico. Additionally, we ensured that the protein concentrations used were within the physiologically relevant range (45). Specifically, we used 100 nM XMAP215 and 200 nM EB1 to increase growth rates to the same extent as in our simulations (34, 36). In the presence of EB1, CLASP2 strongly promotes plus-end stabilization at nanomolar concentrations; we therefore used 20 nM CLASP2, which is predicted to have a saturating effect in our in vitro assay (37). Finally, to induce frequent catastrophes at the minus end, we used a high concentration of MCAK (200 nM). Consistent with our predictions, we found that the plus ends exhibited large positive flux (29.8 ± 2.0 nm/s, mean ± SEM, n = 48; Fig. 4 *A*–*C* and Movie S6), while minus ends exhibited net negative flux (−8.8 ± 1.1, mean ± SEM, n = 48; Fig. 4 *A*–*C*). The vast majority (98%) of the observed microtubules were classified as plus-end-leading treadmilling (Fig. 4*D*). These experimental results corroborated our in silico predictions for the combined effects of XMAP215, EB1, CLASP2, and MCAK on microtubule dynamics. Therefore, we have demonstrated that a multicomponent system of stabilizing, destabilizing and growth-promoting MAPs can reconstitute robust, plus-end-leading microtubule treadmilling.

Discussion

In this study, we have reconstituted cellular-like microtubule treadmilling in vitro. Using the power of predictive computational modeling, combined with highly controlled experiments employing

purified proteins, we showed how MAPs can tune microtubule dynamics to give rise to complex polymer behavior. We learned that robust, plus-end-leading microtubule treadmilling relies on the action of MAPs, as no concentration of soluble tubulin alone permits the sustained, simultaneous plus-end assembly and minus-end disassembly required for persistent treadmilling toward microtubule plus ends. However, none of the MAPs we investigated is sufficient for inducing robust plus-end-leading treadmilling on its own. Importantly, when combined, MAPs can have nonadditive, synergistic, or antagonistic effects on microtubule dynamics (36–38, 46–50); in our simulations, we took into account previously reported nonadditive effects of combinations of the MAPs we used in this study (36–38). We showed that robust plus-end growth can be achieved even at low tubulin concentrations through the combined polymerase and rescue activities of XMAP215, EB1, and CLASP2. However, minus ends are inherently more stable; therefore, minus-end destabilization necessitates the action of a potent depolymerase (29, 44, 51). Indeed, in our reconstitution, we found that the kinesin-13 MCAK is essential for treadmilling. In cells, minus ends can be protected against depolymerase activity by minus-end-targeted proteins from the CAMSAP family and potentially other factors (7, 44). Accordingly, depletion of Patronin, a *Drosophila* member of the CAMSAP family, resulted in observations of treadmilling microtubules in S2 cells (13). Therefore, the shift in balance between minus-end stabilization and destabilization ultimately dictates conditions favorable for microtubule treadmilling.

Microtubule turnover is essential for the remodeling of cytoskeletal networks in fundamental cellular processes. Even cytoskeletal structures with defined steady-state architectures, such as the mitotic spindle, exhibit continuous polymer turnover. Although the mechanisms underlying the poleward streaming of microtubules within the spindle are not fully understood, simultaneous microtubule polymerization at kinetochores and depolymerization at the poles, a form of treadmilling, may contribute to poleward flux (20). Notably, all of the proteins used in our reconstitution of treadmilling play important roles in the spindle architecture and have been implicated in the poleward flux (52–54). In another context, the ability of individual microtubules to treadmill can provide means to erase the defects and post-translational modifications encoded in the microtubule lattice, thus allowing the cell to rewrite the tubulin code (55–58). More generally, treadmilling is a minus-end mechanism of microtubule turnover and translocation that can be employed for global network reorganization in processes such as cell motility and differentiation. Our minimal-component reconstitution demonstrates how microtubule treadmilling can arise through the concerted actions of regulatory factors. To that end, our work provides a deeper understanding of how active polymer systems can be tuned to give rise to robust yet dynamic cytoskeletal architectures.

Materials and Methods

DNA Constructs. The cDNA encoding full-length human CLASP2γ (NCBI accession no. NM_001207044.1) was a gift from I. Kaverina, Vanderbilt University, Nashville, TN. MCAK-6His and XMAP215-7His insect expression constructs were gifts from G. Brouhard, McGill University, Montreal, QC, Canada (40, 59). *Drosophila* rigor 6His-kinesin-1(R210A) bacterial expression construct was a kind gift from W. Hancock, The Pennsylvania State University, State College, PA (60).

Protein Preparation. Bovine brain tubulin was purified using the high-molarity method (61). Tubulin was labeled with TAMRA, Alexa Fluor 488, and Alexa Fluor 647 (Invitrogen) according to the standard protocols, as previously described (30). Fluorescently labeled tubulin was typically used at a ratio of between 5% and 10% of the total tubulin when growing dynamic microtubule extensions.

The 6His-EB1 and 6His-CLASP2γ were expressed and purified as previously described (36, 37). 6His-kinesin-1(R210A) was expressed in BL21(DE3) *Escherichia coli* cells. The bacterial cell pellet was resuspended in lysis buffer [50 mM sodium phosphate buffer (pH 7.4), 300 mM NaCl, 1 mM $MgCl_2$, 0.1 mM adenosine 5′-triphosphate (ATP), 1 mM dithiothreitol (DTT), and 40 mM imidazole] containing protease inhibitors, lysozyme (1 mg/mL), and a universal nuclease (25 U/mL ; Pierce) and incubated for 1 h at 4 °C. The lysate was further processed by Dounce homogenization and sonication and clarified by centrifugation for 30 min at 4 °C and 35,000 rpm in a Beckman L90K Optima and 50.2 Ti rotor. The clarified lysate was applied to a HisTrapHP column (GE Lifesciences) according to the manufacturer's instructions and eluted with 50 mM sodium phosphate buffer (pH 7.4), 300 mM NaCl, 1 mM $MgCl_2$, 0.1 mM ATP, 1 mM DTT, and 500 mM imidazole. Peak elution fractions were pooled and buffer exchanged into storage buffer [50 mM sodium phosphate buffer (pH 7.4), 300 mM NaCl, 1 mM $MgCl_2$, 0.5 mM ATP, 1 mM DTT, and 10% sucrose] using an Amicon centrifugal filter.

MCAK-6His and XMAP215-7His were expressed in baculovirus-infected Sf9 insect cells using the Bac-to-Bac system according to the manufacturer's instructions (Invitrogen) and purified by adapting previously published protocols (34, 40, 59). Briefly, baculovirus-infected insect cells (BIIC) stocks were prepared and used to infect Sf9 cells at a density of 10^6 viable cells per mL with BIIC stocks at a ratio of 10^{-4} BIIC:total culture volume (62). Cells were harvested 4 d after infection. Insect cell pellets were lysed by one freeze–thaw cycle and Dounce homogenizing in lysis buffer containing protease inhibitors. MCAK-6His cell pellets were lysed in 50 mM 4-(2-hydroxyethyl)-1-piperazineethanesulfonic acid (HEPES) (pH 7.5), 150 mM NaCl, 5% glycerol, 0.1% Tween-20, 1.5 mM $MgCl_2$, 1 mM DTT, and 0.5 mM ATP. XMAP215-7His cell pellets were lysed in 50 mM HEPES (pH 7.5), 50 mM NaCl, 5% glycerol, 0.1% Triton-X-100, and 1 mM DTT. Genomic DNA was sheared by passing the lysate through an 18-gauge needle. Crude lysate was clarified by centrifugation as described above and applied to a HisTrapHP column (GE Lifesciences). His-tagged proteins were eluted with the following elution buffers: 50 mM HEPES (pH 7.5), 150 mM NaCl, 5% glycerol, 1.5 mM $MgCl_2$, 1 mM DTT, 0.5 mM ATP, and 300 mM imidazole for MCAK-6His and 50 mM HEPES (pH 7.5), 300 mM NaCl, 10% glycerol, 1 mM DTT, and 500 mM imidazole for XMAP215-7His. For each protein, peak elution fractions were pooled and applied to a Superdex 200 Increase 10/300 GL size-exclusion column (GE Healthcare) in the following buffers: 20 mM HEPES (pH 7.5), 150 mM NaCl, 10% (vol/vol) glycerol, 1 mM $MgCl_2$, 1 mM DTT, and 0.5 mM ATP for MCAK-6His and 10 mM Tris·HCl (pH 6.6), 10 mM Bis-Tris, 100 mM KCl, 10% glycerol, and 1 mM DTT for XMAP215-7His. Purified proteins were snap-frozen in liquid nitrogen as single-use aliquots.

Dynamic Microtubule Assay. Microscope chambers were constructed as previously described (30). In brief, 22- × 22-mm and 18- × 18-mm coverslips were separated by strips of Parafilm to create a narrow channel for the exchange of solution (30). For the "seeded" assay, guanosine-5′-[(α,β)-methyleno]triphosphate (GMPCPP)-stabilized microtubules were prepared according to standard protocols (30, 63) and dynamic microtubule extensions were polymerized from surface-immobilized GMPCPP-stabilized templates as previously described (30). For the "seedless" assay, dynamic microtubules were prenucleated in solution with GTP and then attached to coverslips by surface-bound rigor kinesin-1 motor protein [6His-kinesin-1(R210A)]. To prepare the rigor kinesin-1–coated coverslips, silanized coverslips were first rinsed with BRB80 [80 mM piperazine-*N*,*N*′-bis(2-ethanesulfonic acid), 1 mM MgCl2, and 1 mM EGTA (ethylene glycol-bis(β-aminoethyl ether)-*N*,*N*,*N*′,*N*′-tetraacetic acid) (pH 6.8) with KOH] then incubated with anti-His antibody (10 μg/mL, ab18184; Abcam) for 5 min and blocked with 1% pluronic F127 in BRB80 for 30 min. Next, the anti-His antibody-coated coverslips were incubated with 2 μg/mL rigor kinesin-1 in the presence of 8 mg/mL casein in BRB80 for 15 min and then blocked with 1 mg/mL His-BSA for 10 min. Note that for the seedless assay with tubulin alone, rigor kinesin-1 was nonspecifically adsorbed to coverslips based on previously published protocols for microtubule gliding assays (64). In this case, coverslips were blocked with 1 mg/mL casein in BRB80 for 5 min, the rigor kinesin-1 was adsorbed to the surface by incubating for 10 min in the presence of 1 mg/mL casein, and the surface was washed with BRB80 including 1 mg/mL casein.

Imaging buffer containing concentrations of tubulin ranging from 4 to 15 μM tubulin, 1 mM GTP, and proteins at the concentrations indicated in the text were introduced into the imaging chamber. The imaging buffer consisted of BRB80 supplemented with 40 mM glucose, 40 μg/mL glucose oxidase, 16 μg/mL catalase, 0.5 mg/mL casein, 50 mM KCl, and 10 mM DTT. Additionally, 0.1% methylcellulose was used in the seeded assay to reduce thermal fluctuations of long microtubule extensions, and 1 mM ATP was included whenever MCAK was used. In the seedless assay microtubules were prenucleated in the channels using 12 to 15 μM A647- or TAMRA-labeled GTP-tubulin for 10 to 15 min, and then the solution was exchanged for 4 to

6 μM A488-labeled GTP-tubulin and additional proteins when used, as indicated in the text.

Microscopy. Imaging of microtubule dynamics in vitro was performed using a Nikon Eclipse Ti microscope equipped with a 100×/1.49 numerical aperture TIRF objective, Andor iXon Ultra EM-CCD (electron-multiplying charge-coupled device), and NEO sCMOS (scientific complementary metal-oxide semiconductor) cameras; 488-, 561-, and 640-nm solid-state lasers (Nikon Lu-NA); Finger Lakes Instruments HS-625 high-speed emission filter wheel; and standard filter sets. An objective heater was used to maintain the sample at 35 °C. Images were acquired using NIS-Elements (Nikon). Microtubules were imaged for 30 min with 2-s intervals for Figs. 1 and 4 and for 45 min postdilution with 15-s intervals for Fig. 2.

Image and Data Analysis. Image analysis was performed using Fiji (65). Time-lapse of TIRF images were drift-corrected using the ImageJ plugins Template Matching and Slice Alignment (66) and Image Stabilizer (67). Kymographs were created using a custom ImageJ macro based on the Multi Kymograph plugin. Plus and minus ends were distinguished based on their growth rates: faster-growing ends were identified as the plus ends and the slower-growing ends as the minus ends. Microtubule dynamics were characterized as previously described (31). Briefly, growth and shrinkage speeds were quantified as the change in length divided by time. Catastrophe frequency was calculated as the number of catastrophe events divided by total time in growth. Rescue per shrinkage length (r_{res}) was calculated as the number of rescues divided by total length of shrinkage. Rescue frequency was calculated by multiplying the shrinkage speed by rescue per shrinkage length ($f_{res} = v_s r_{res}$).

For the seedless assay with tubulin alone, the first 10 min of the 45-min-long movies were not analyzed to ensure the analysis was restricted to steady-state polymer behavior (*SI Appendix*, Fig. S1). To track the position of the microtubule end over time, the beginning and the end of each growth and shrinkage event were detected manually from the kymographs, and the intermediate end coordinates were assigned using interpolation assuming linear rates, with a custom MATLAB code. To correct for possible residual microtubule gliding, two-color kymographs were used. The corrected microtubule end coordinates were then exported as data files for further analysis. The average gliding rates determined were negligible (~1 nm/s). Therefore, for seedless assay with MAPs, the microtubule gliding was neglected.

The subunit flux was determined empirically, except for the seeded assay with tubulin alone. For the seeded assay, flux was determined analytically at a population level. Briefly, we calculated the rate of subunit addition and loss (i.e., flux $J_{analytical}$), as a function of tubulin concentration for both plus and minus ends using the measured dynamic parameters. An analytical expression used by earlier studies (29, 32, 33) is given by

$$J_{\text{analytical}} = v_g p_g - v_s p_s \equiv \frac{v_g f_{res} - v_s f_{cat}}{f_{res} + f_{cat}},$$

where v_g and v_s are the growth and shrinkage rates, p_g and p_s are the fraction of time spent in growth and shrinkage phases, and f_{cat} and f_{res} are the catastrophe and rescue frequencies, respectively. This expression holds true as long as a microtubule end can be classified as either growing or shrinking at any given time. Given $f_{res} = v_s r_{res}$, where r_{res} is rescue per shrinkage length, the errors for the flux values were calculated from individual dynamics parameters using error propagation:

$$J = \frac{v_g v_s r_{res} - v_s f_{cat}}{v_s r_{res} + f_{cat}}$$

$$\delta J = \sqrt{\left(\frac{\partial J}{\partial v_g}\delta v_g\right)^2 + \left(\frac{\partial J}{\partial v_s}\delta v_s\right)^2 + \left(\frac{\partial J}{\partial f_{cat}}\delta f_{cat}\right)^2 + \left(\frac{\partial J}{\partial r_{res}}\delta r_{res}\right)^2}$$

$$\frac{\partial J}{\partial v_g} = \frac{v_s r_{res}}{v_s r_{res} + f_{cat}}$$

$$\frac{\partial J}{\partial v_s} = \frac{f_{cat}(v_g r_{res} - f_{cat})}{(v_s r_{res} + f_{cat})^2}$$

$$\frac{\partial J}{\partial f_{cat}} = -\frac{v_s r_{res}(v_g + v_s)}{(v_s r_{res} + f_{cat})^2}$$

$$\frac{\partial J}{\partial r_{res}} = \frac{v_s f_{cat}(v_g + v_s)}{(v_s r_{res} + f_{cat})^2},$$

where δ is the error and ∂ represents partial derivative.

The net flux of the tubulin subunits onto the microtubule is given by

$$J^{\text{microtubule}} = J^{\text{plus}} + J^{\text{minus}}.$$

The positive flux at one end indicates that microtubules exhibit net growth at this given end. Similarly, the negative flux at an end implies net shrinkage. Note that the flux is expected to follow a linear trend as a function of tubulin concentration in the positive flux range but becomes nonlinear in the regime of tubulin concentration for which the flux is negative (33). Furthermore, the negative flux values we determined for low tubulin concentrations have relatively large errors due to the larger uncertainty in the measured dynamics parameters in this tubulin concentration regime. This analytical method of flux calculation allows us to estimate negative fluxes at low tubulin concentrations that cannot be directly observed in the seeded assay. Negative flux can only be directly measured by prepolymerizing microtubules and then diluting the tubulin concentration to the negative flux regime, as we did for all of our subsequent seedless assay simulations and experiments. For the seeded assay, the tubulin concentrations at which the flux crosses the zero value were determined using weighted fits of the calculated flux values over the range of concentrations for which the flux is expected to follow a linear trend (33) (7 to 12 μM for the plus end and 5 to 12 μM for the minus end).

With the exception of the seeded assay with tubulin alone, in all other instances the flux at individual microtubule ends was determined empirically. Briefly, we measured the magnitude of net flux of subunits onto polymer ends in a given time period by dividing the total change in length (gain or loss) by the total time:

$$J_{\text{empirical}} = \frac{x_f - x_i}{t_f - t_i} = \frac{\Delta x}{\Delta t},$$

where x_i (x_f) is the initial (final) position of a given end at time t_i (t_f). Δx is the net polymer length gain/loss, while Δt is the "observation time." Net growth is associated with positive flux, while net shrinkage is associated with negative flux. Similarly, as for the analytically calculated flux, the total flux on the microtubule is the sum of the fluxes at plus and minus ends. Microtubules were then grouped into four dynamic modes based on their fluxes at the ends. To determine the extent to which our classification into dynamic modes depends on the time window size used, we calculated the net flux using a range of window sizes (1 to 30 min) and then classified each dynamic microtubule segment into a dynamic mode (*SI Appendix*, Fig. S1). One of the four dynamic modes was assigned to the middle time point of the sliding window, then the window was moved by one time frame to determine the next dynamic mode. As expected, the classification coincided with individual events of microtubule catastrophe and shrinkage for small window sizes (<5 min) and therefore did not capture the global polymer behavior. Global behavior was captured using larger window sizes, reaching a relative plateau with window sizes greater than ~10 min. Therefore, for further analysis and classification, we used the entire polymer lifetime, considering microtubules that were observed for >10 min.

Computational Model. Microtubules were modeled as one-dimensional rigid rods, not interacting with each other. The growth and shrinkage speeds, and catastrophe and rescue frequencies were given as inputs. The dynamics of the two ends were independently simulated with a time step of $\tau = 10^{-5}$ s. In every time step, a given microtubule end is in either a growing or shrinking phase: The pause state was not included in the model. During each time step, the given microtubule end grows (or shrinks) if a random number, p_1 in the interval [0,1] satisfies

$$p_1 \leq 1 - e^{-\tau v/d},$$

where v is growth (shrinkage) rate, $d = 8$ nm/13 is the dimer size. Similarly, a given microtubule end undergoes catastrophe (or rescue) if a random number, p_2 in the interval [0,1] satisfies

$$p_2 \leq f\tau,$$

where f is the catastrophe (rescue) frequency.

At the beginning of the simulation, and at the onset of each new growth (shrinkage) event, a new growth (shrinkage) speed and catastrophe (rescue) frequency was chosen from Gaussian distributions with means as inputted values and SD of 10% of the mean value. If a negative random number was generated, a new number was chosen from the distribution to ensure positive parameter values.

For visualization purposes, and to better mimic our in vitro TIRF dynamics assay, microtubules were randomly placed in a two-dimentional surface with random angles ($0 \leq \theta \leq 2\Pi$), with their center point coordinates lying within a 100- × 100-μm field of view. The computational model was developed in Fortran 90. The realizations and post processing were parallelized using GNU parallel (68) when applicable.

To assess our computational model, we first compared the input parameters with the simulation outputs for these parameters (*SI Appendix*, Fig. S2). Fifty microtubules with initial lengths of 15 ± 2 μm were simulated for 30 min. After the simulations were complete, we calculated growth/shrinkage rate for each individual growth/shrinkage phase of a given simulated microtubule. We then performed a Gaussian fit to the cumulative distribution $\left(CDF(v) = \frac{1}{2}\left[1 + erf\left(\frac{v - \langle v \rangle}{\sigma_v \sqrt{2}}\right)\right]\right)$ of individual growth/shrinkage speeds from all of the simulated microtubules in a given realization to obtain the population mean and SD. Catastrophe/rescue frequencies were determined by fitting an exponential decay function to the cumulative distribution ($CDF(t) = 1 - e^{-ft}$) of individual lifetimes of growth/shrinkage events from all simulated microtubules in a given realization. Weighted mean values were determined from 10 independent simulation realizations, with weights being the inverse of half of the 95% confidence interval. Data were fitted in MATLAB using the curve fitting tool.

Data Availability Statement. Additional data that support the findings of this study are available in *SI Appendix*. All simulation codes used in this study are available on GitHub (https://github.com/ZanicLab).

ACKNOWLEDGMENTS. We thank J. Alper, S. Bechstedt, G. Brouhard, W. Hancock, and R. Ohi for critical feedback; the members of the Vanderbilt Microtubule and Motors Club, particularly D. Burnette, I. Kaverina, and M. Tyska, as well as the members of the M.Z. laboratory, for discussions and feedback; the Hancock laboratory, Pennsylvania State University, for the gift of rigor kinesin-1 construct; and the Brouhard laboratory, McGill University, for the gift of XMAP215 and MCAK constructs. We acknowledge support from NIH Grant R35GM119552, Searle Scholars Program and Human Frontier Science Program Career Development Award to M.Z., Integrated Biological Systems Training in Oncology T32 Training Grant CA119925 to E.J.L., and American Heart Association Predoctoral Fellowship 19PRE34380083 to V.J.F.

1. B. Bugyi, M. F. Carlier, Control of actin filament treadmilling in cell motility. *Annu. Rev. Biophys.* **39**, 449–470 (2010).
2. A. W. Bisson-Filho *et al*., Treadmilling by FtsZ filaments drives peptidoglycan synthesis and bacterial cell division. *Science* **355**, 739–743 (2017).
3. X. Deng *et al*., Four-stranded mini microtubules formed by *Prosthecobacter* BtubAB show dynamic instability. *Proc. Natl. Acad. Sci. U.S.A.* **114**, E5950–E5958 (2017).
4. V. Chaikeeratisak *et al*., Viral capsid trafficking along treadmilling tubulin filaments in bacteria. *Cell* **177**, 1771–1780 e12 (2019).
5. H. P. Erickson, Microtubule assembly from single flared protofilaments-forget the cozy corner? *Biophys. J.* **116**, 2240–2245 (2019).
6. T. Mitchison, M. Kirschner, Dynamic instability of microtubule growth. *Nature* **312**, 237–242 (1984).
7. A. Akhmanova, M. O. Steinmetz, Microtubule minus-end regulation at a glance. *J. Cell Sci.* **132**, jcs227850 (2019).
8. V. I. Rodionov, G. G. Borisy, Microtubule treadmilling in vivo. *Science* **275**, 215–218 (1997).
9. S. L. Shaw, R. Kamyar, D. W. Ehrhardt, Sustained microtubule treadmilling in Arabidopsis cortical arrays. *Science* **300**, 1715–1718 (2003).
10. C. M. Waterman-Storer, E. D. Salmon, Actomyosin-based retrograde flow of microtubules in the lamella of migrating epithelial cells influences microtubule dynamic instability and turnover and is associated with microtubule breakage and treadmilling. *J. Cell Biol.* **139**, 417–434 (1997).
11. R. L. Margolis, L. Wilson, Microtubule treadmilling: What goes around comes around. *BioEssays* **20**, 830–836 (1998).
12. T. Wittmann, G. M. Bokoch, C. M. Waterman-Storer, Regulation of leading edge microtubule and actin dynamics downstream of Rac1. *J. Cell Biol.* **161**, 845–851 (2003).
13. S. S. Goodwin, R. D. Vale, Patronin regulates the microtubule network by protecting microtubule minus ends. *Cell* **143**, 263–274 (2010).
14. G. Chomicki, R. Wightman, S. R. Turner, A specific class of short treadmilling microtubules enhances cortical microtubule alignment. *Mol. Plant* **9**, 1214–1216 (2016).
15. C. M. Waterman-Storer, E. D. Salmon; C. M. Waterman-Storer, Microtubule dynamics: Treadmilling comes around again. *Curr. Biol.* **7**, R369–R372 (1997).
16. T. J. Keating, J. G. Peloquin, V. I. Rodionov, D. Momcilovic, G. G. Borisy, Microtubule release from the centrosome. *Proc. Natl. Acad. Sci. U.S.A.* **94**, 5078–5083 (1997).
17. V. Rodionov, E. Nadezhdina, G. Borisy, Centrosomal control of microtubule dynamics. *Proc. Natl. Acad. Sci. U.S.A.* **96**, 115–120 (1999).
18. S. L. Shaw, J. Lucas, Intrabundle microtubule dynamics in the Arabidopsis cortical array. *Cytoskeleton (Hoboken)* **68**, 56–67 (2011).
19. I. A. Vorobjev, V. I. Rodionov, I. V. Maly, G. G. Borisy, Contribution of plus and minus end pathways to microtubule turnover. *J. Cell Sci.* **112**, 2277–2289 (1999).
20. L. Cassimeris, Cell division: Eg'ing on microtubule flux. *Curr. Biol.* **14**, R1000–R1002 (2004).
21. K. W. Farrell, M. A. Jordan, H. P. Miller, L. Wilson, Phase dynamics at microtubule ends: The coexistence of microtubule length changes and treadmilling. *J. Cell Biol.* **104**, 1035–1046 (1987).
22. R. L. Margolis, L. Wilson, Opposite end assembly and disassembly of microtubules at steady state in vitro. *Cell* **13**, 1–8 (1978).
23. D. Panda, H. P. Miller, L. Wilson, Rapid treadmilling of brain microtubules free of microtubule-associated proteins in vitro and its suppression by tau. *Proc. Natl. Acad. Sci. U.S.A.* **96**, 12459–12464 (1999).
24. S. Grego, V. Cantillana, E. D. Salmon, Microtubule treadmilling in vitro investigated by fluorescence speckle and confocal microscopy. *Biophys. J.* **81**, 66–78 (2001).
25. H. Hotani, T. Horio, Dynamics of microtubules visualized by darkfield microscopy: Treadmilling and dynamic instability. *Cell Motil. Cytoskeleton* **10**, 229–236 (1988).
26. T. Manna, D. Thrower, H. P. Miller, P. Curmi, L. Wilson, Stathmin strongly increases the minus end catastrophe frequency and induces rapid treadmilling of bovine brain microtubules at steady state in vitro. *J. Biol. Chem.* **281**, 2071–2078 (2006).
27. S. W. Rothwell, W. A. Grasser, D. B. Murphy, Direct observation of microtubule treadmilling by electron microscopy. *J. Cell Biol.* **101**, 1637–1642 (1985).
28. A. Akhmanova, M. O. Steinmetz, Control of microtubule organization and dynamics: Two ends in the limelight. *Nat. Rev. Mol. Cell Biol.* **16**, 711–726 (2015).
29. R. A. Walker *et al*., Dynamic instability of individual microtubules analyzed by video light microscopy: Rate constants and transition frequencies. *J. Cell Biol.* **107**, 1437–1448 (1988).
30. C. Gell *et al*., Microtubule dynamics reconstituted in vitro and imaged by single-molecule fluorescence microscopy. *Methods Cell Biol.* **95**, 221–245 (2010).
31. M. Zanic, Measuring the effects of microtubule-associated proteins on microtubule dynamics in vitro. *Methods Mol. Biol.* **1413**, 47–61 (2016).
32. F. Verde, M. Dogterom, E. Stelzer, E. Karsenti, S. Leibler, Control of microtubule dynamics and length by cyclin A- and cyclin B-dependent kinases in Xenopus egg extracts. *J. Cell Biol.* **118**, 1097–1108 (1992).
33. A. J. Mauro, E. M. Jonasson, H. V. Goodson, Relationship between dynamic instability of individual microtubules and flux of subunits into and out of polymer. *Cytoskeleton (Hoboken)* **76**, 495–516 (2019).
34. G. J. Brouhard *et al*., XMAP215 is a processive microtubule polymerase. *Cell* **132**, 79–88 (2008).
35. D. L. Gard, M. W. Kirschner, A microtubule-associated protein from Xenopus eggs that specifically promotes assembly at the plus-end. *J. Cell Biol.* **105**, 2203–2215 (1987).
36. M. Zanic, P. O. Widlund, A. A. Hyman, J. Howard, Synergy between XMAP215 and EB1 increases microtubule growth rates to physiological levels. *Nat. Cell Biol.* **15**, 688–693 (2013).
37. E. J. Lawrence, G. Arpag, S. R. Norris, M. Zanic, Human CLASP2 specifically regulates microtubule catastrophe and rescue. *Mol. Biol. Cell* **29**, 1168–1177 (2018).
38. A. Aher *et al*., CLASP suppresses microtubule catastrophes through a single TOG domain. *Dev. Cell* **46**, 40–58 e8 (2018).
39. E. J. Lawrence, M. Zanic, Rescuing microtubules from the brink of catastrophe: CLASPs lead the way. *Curr. Opin. Cell Biol.* **56**, 94–101 (2019).
40. J. Helenius, G. Brouhard, Y. Kalaidzidis, S. Diez, J. Howard, The depolymerizing kinesin MCAK uses lattice diffusion to rapidly target microtubule ends. *Nature* **441**, 115–119 (2006).
41. A. Desai, S. Verma, T. J. Mitchison, C. E. Walczak, Kin I kinesins are microtubule-destabilizing enzymes. *Cell* **96**, 69–78 (1999).
42. M. K. Gardner, M. Zanic, C. Gell, V. Bormuth, J. Howard, Depolymerizing kinesins Kip3 and MCAK shape cellular microtubule architecture by differential control of catastrophe. *Cell* **147**, 1092–1103 (2011).
43. P. Bieling *et al*., Reconstitution of a microtubule plus-end tracking system in vitro. *Nature* **450**, 1100–1105 (2007).
44. C. Strothman *et al*., Microtubule minus-end stability is dictated by the tubulin off-rate. *J. Cell Biol.* **218**, 2841–2853 (2019).
45. D. N. Itzhak, S. Tyanova, J. Cox, G. H. Borner, Global, quantitative and dynamic mapping of protein subcellular localization. *eLife* **5**, e16950 (2016).
46. W. Li *et al*., Reconstitution of dynamic microtubules with Drosophila XMAP215, EB1, and Sentin. *J. Cell Biol.* **199**, 849–862 (2012).
47. T. Moriwaki, G. Goshima, Five factors can reconstitute all three phases of microtubule polymerization dynamics. *J. Cell Biol.* **215**, 357–368 (2016).
48. N. Yu *et al*., Isolation of functional tubulin dimers and of tubulin-associated proteins from mammalian cells. *Curr. Biol.* **26**, 1728–1736 (2016).
49. S. Montenegro Gouveia *et al*., In vitro reconstitution of the functional interplay between MCAK and EB3 at microtubule plus ends. *Curr. Biol.* **20**, 1717–1722 (2010).
50. K. Kinoshita, I. Arnal, A. Desai, D. N. Drechsel, A. A. Hyman, Reconstitution of physiological microtubule dynamics using purified components. *Science* **294**, 1340–1343 (2001).
51. P. T. Tran, R. A. Walker, E. D. Salmon, A metastable intermediate state of microtubule dynamic instability that differs significantly between plus and minus ends. *J. Cell Biol.* **138**, 105–117 (1997).
52. H. Maiato, A. Khodjakov, C. L. Rieder, Drosophila CLASP is required for the incorporation of microtubule subunits into fluxing kinetochore fibres. *Nat. Cell Biol.* **7**, 42–47 (2005).
53. G. C. Rogers *et al*., Two mitotic kinesins cooperate to drive sister chromatid separation during anaphase. *Nature* **427**, 364–370 (2004).

54. I. Kronja, A. Kruljac-Letunic, M. Caudron-Herger, P. Bieling, E. Karsenti, XMAP215-EB1 interaction is required for proper spindle assembly and chromosome segregation in Xenopus egg extract. *Mol. Biol. Cell* **20**, 2684–2696 (2009).
55. K. J. Verhey, J. Gaertig, The tubulin code. *Cell Cycle* **6**, 2152–2160 (2007).
56. C. Janke, The tubulin code: Molecular components, readout mechanisms, and functions. *J. Cell Biol.* **206**, 461–472 (2014).
57. L. Schaedel *et al*., Microtubules self-repair in response to mechanical stress. *Nat. Mater.* **14**, 1156–1163 (2015).
58. C. Aumeier *et al*., Self-repair promotes microtubule rescue. *Nat. Cell Biol.* **18**, 1054–1064 (2016).
59. M. Wieczorek, S. Bechstedt, S. Chaaban, G. J. Brouhard, Microtubule-associated proteins control the kinetics of microtubule nucleation. *Nat. Cell Biol.* **17**, 907–916 (2015).
60. C. M. Farrell, A. T. Mackey, L. M. Klumpp, S. P. Gilbert, The role of ATP hydrolysis for kinesin processivity. *J. Biol. Chem.* **277**, 17079–17087 (2002).
61. M. Castoldi, A. V. Popov, Purification of brain tubulin through two cycles of polymerization-depolymerization in a high-molarity buffer. *Protein Expr. Purif.* **32**, 83–88 (2003).
62. D. J. Wasilko *et al*., The titerless infected-cells preservation and scale-up (TIPS) method for large-scale production of NO-sensitive human soluble guanylate cyclase (sGC) from insect cells infected with recombinant baculovirus. *Protein Expr. Purif.* **65**, 122–132 (2009).
63. A. A. Hyman, S. Salser, D. N. Drechsel, N. Unwin, T. J. Mitchison, Role of GTP hydrolysis in microtubule dynamics: Information from a slowly hydrolyzable analogue, GMPCPP. *Mol. Biol. Cell* **3**, 1155–1167 (1992).
64. K. J. Mickolajczyk *et al*., Kinetics of nucleotide-dependent structural transitions in the kinesin-1 hydrolysis cycle. *Proc. Natl. Acad. Sci. U.S.A.* **112**, E7186–E7193 (2015).
65. J. Schindelin *et al*., Fiji: An open-source platform for biological-image analysis. *Nat. Methods* **9**, 676–682 (2012).
66. Q. Tseng *et al*., A new micropatterning method of soft substrates reveals that different tumorigenic signals can promote or reduce cell contraction levels. *Lab Chip* **11**, 2231–2240 (2011).
67. K. Li, The image stabilizer plugin for ImageJ. https://www.cs.cmu.edu/~kangli/code/Image_Stabilizer.html (2008).
68. O. Tange, *GNU Parallel 2018*, (Ole Tange, 2018).